Chapter 2

Smeagol: Density Functional Theory and NEGF's

2.1 Introduction: The many-body problem

In solid state physics one is interested in systems comprising many atoms, and consequently many electrons. Therefore the description of the electronic structure of molecules and solids entails the correct characterisation of a large number of particles: electrons and nucleons. In all but a handful of cases the number of particles involved is prohibitive. In fact, the problem involving many electrons is unsolvable analytically, and exact numerical solutions are computationally feasible for a few electrons. As often is the case one must rely on approximations and ultimately on numerical methods to obtain the desired properties.

In many-particle systems one must solve an eigenvalue problem for the energy E in the form

$$\hat{\mathcal{H}}\Psi = E\Psi \tag{2.1}$$

where $\hat{\mathcal{H}}$ is the quantum mechanical Hamiltonian of the form:

$$\begin{aligned}\hat{\mathcal{H}} &= \sum_i^{N_e} \frac{-\hbar^2}{2m_e}\nabla^2_{\vec{r}_i} + \sum_I^{N_N} \frac{-\hbar^2}{2M_I}\nabla^2_{\vec{R}_I} + \frac{1}{2}\sum_{I\neq J}^{N_N} \frac{e^2 Z_J Z_I}{\left|\vec{\mathbf{R}}_I - \vec{\mathbf{R}}_J\right|} - \\ &- \frac{1}{2}\sum_{i,I}^{N_e,N_N} \frac{e^2 Z_I}{\left|\vec{\mathbf{r}}_i - \vec{\mathbf{R}}_I\right|} + \frac{1}{2}\sum_{i\neq j}^{N} \frac{Ze^2}{|\vec{\mathbf{r}}_i - \vec{\mathbf{r}}_j|},\end{aligned} \tag{2.2}$$

where $\vec{\mathbf{x}}_i$ is the position operator for the i-th electron and $\vec{\mathbf{R}}_I$ the analogous position operator for I-th nucleus.[1] In equation (2.2), the first term represents the kinetic energy of the electrons of mass m_e, the second the kinetic energy of the nuclei - with

[1] We consider the nucleus as a point charge $Z_I\,|e|$, with $|e|$ the electronic charge.

mass M_I; the third the Coulomb interaction between different nuclei; the fourth, the electrostatic attraction between *nuclei* and electrons and finally the fifth term is the electron-electron interaction.

In most solid state problems N_e and N_N are of the order of 10^{23}-10^{26} particles. Therefore the many-body wavefunction

$$\Psi = \Psi\left(\vec{\mathbf{x}}_1, \vec{\mathbf{x}}_2..., \vec{\mathbf{x}}_i, ..., \vec{\mathbf{x}}_{N_e}; \vec{\mathbf{X}}_1, \vec{\mathbf{X}}_2..., \vec{\mathbf{X}}_i, ..., \vec{\mathbf{X}}_{N_N}\right)^{2} \tag{2.3}$$

is a function of an insurmountable number of variables.

In order to solve such a problem we must start by making a few assumptions that allow us to reduce the number of variables involved. The first assumption comes from the fact that the masses of the nuclei are much larger than those of the electrons. In that case we can assume that the Hamiltonian is separable. From a classical perspective this is equivalent to considering the nuclei to move at a much slower speed than the electrons. From the electrons' reference point they are almost stationary. Hence, one can separate the electronic wavefunction from that of the nuclei

$$\Psi = \Psi^e\left(\{\vec{\mathbf{x}}_i\}\right) \times \Psi^N\left(\{\vec{\mathbf{X}}_i\}\right). \tag{2.4}$$

Within this approximation (the Born-Oppenheimer approximation [106]) if one knows the positions of the nuclei, he will only need to worry about solving for the electronic part of the wavefunction. Hence, the Schrödinger equations (2.1) and (2.2) reduce to

$$\hat{\mathcal{H}}\Psi = \left[\hat{\mathcal{H}}^e + \hat{\mathcal{H}}^N\right]\Psi^e\Psi^N, \tag{2.5}$$

$$\hat{\mathcal{H}}^e\Psi^e = E\left(\{\vec{\mathbf{X}}_i\}\right)\Psi^e, \tag{2.6}$$

$$\hat{\mathcal{H}}^e = \hat{T}_e\left(\{\vec{\mathbf{x}}_i\}\right) + \hat{V}_{ee}\left(\{\vec{\mathbf{x}}_i\}\right) + \hat{V}_{eN}\left(\{\vec{\mathbf{x}}_i\}; \{\vec{\mathbf{X}}_i\}\right), \tag{2.7}$$

where

$$\hat{T}_e\left(\{\vec{\mathbf{x}}_i\}\right) = \sum_i^{N_e} \frac{-\hbar^2}{2m_e}\nabla^2_{\vec{r}_i} \tag{2.8}$$

$$\hat{V}_{ee}\left(\{\vec{\mathbf{x}}_i\}\right) = \frac{1}{2}\sum_{i\neq j}^{N} \frac{e^2}{|\vec{\mathbf{r}}_i - \vec{\mathbf{r}}_j|} \tag{2.9}$$

$$\hat{V}_{eN}\left(\{\vec{\mathbf{x}}_i\}; \{\vec{\mathbf{X}}_i\}\right) = -\frac{1}{2}\sum_{i,I}^{N_e,N_N} \frac{e^2 Z_I}{\left|\vec{\mathbf{r}}_i - \vec{\mathbf{R}}_I\right|}. \tag{2.10}$$

[2]Throughout this chapter we assume that the coordinates $\vec{\mathbf{x}}_i$ comprise both the position $\vec{\mathbf{r}}_i$ as well as the spin coordinates $\vec{s}_i$ ($\vec{\mathbf{X}}_I$, $\vec{\mathbf{R}}_I$ and $\vec{\mathbf{I}}_I$ respectively for the nuclei).

The total electronic energy $E\left(\{\vec{\mathbf{X}}_i\}\right)$ is a function of the position of the nuclei and is calculated for a particular atomic configuration. Such configuration is usually obtained by calculating the atomic forces and relaxing their coordinates using classical equations of motion.

2.1.1 An attempt at solving the many-electron problem

Finding the solution of equation (2.6) is still far from being easy. The main difficulty comes form the second term in this equation, $\hat{V}_{ee}$. Because of this term the problem we cannot write the total many-electron wavefunction as a product of single-particle wavefunctions. In other words, it is not possible to separate the coordinates for each electron and to treat them separately.

One possibility of solving this problem comes from noting that the total electronic wavefunction must be anti-symmetric, since electrons are fermions. Therefore we can propose a solution which is an anti-symmetric product of single particle wavefunctions $\phi_i\left(\{\vec{\mathbf{x}}_j\}\right)$.

$$\Psi^e_{HF} = \frac{1}{N!}\begin{vmatrix} \phi_1\left(\vec{\mathbf{x}}_1\right) & \phi_2\left(\vec{\mathbf{x}}_1\right) & \cdots & \phi_N\left(\vec{\mathbf{x}}_1\right) \\ \phi_1\left(\vec{\mathbf{x}}_2\right) & \phi_2\left(\vec{\mathbf{x}}_2\right) & \cdots & \phi_N\left(\vec{\mathbf{x}}_2\right) \\ \vdots & \vdots & & \vdots \\ \phi_1\left(\vec{\mathbf{x}}_N\right) & \phi_2\left(\vec{\mathbf{x}}_N\right) & \cdots & \phi_N\left(\vec{\mathbf{x}}_N\right) \end{vmatrix} = \frac{1}{N!}\det\left[\phi_i\left(\vec{\mathbf{x}}_j\right)\right]. \tag{2.11}$$

The method that uses the single Slater determinant of form (2.11) as a solution for the wavefunction is known as the Hartree-Fock method [106, 112]. The basis functions $\{\phi_i\left(\{\vec{\mathbf{x}}_j\}\right)\}$ are usually written in terms of linear combinations of Gaussian-type orbitals, *i. e.* localised orbitals. These orbitals are then used to calculate the minima of

$$\delta\left\{\langle\Psi^e|\hat{\mathcal{H}}^e|\Psi^e\rangle - E\langle\Psi^e|\Psi^e\rangle\right\} = 0. \tag{2.12}$$

The equation (2.12) expresses the variational principle over the energy [113].

If a system is periodic, Bloch's theorem [93] significantly reduces the number of degrees of freedom of the problem. However, in large scale electronic structure calculations and in particular in molecular electronics problems Hartree-Fock methods can be extremely expensive in computational terms. The size of a Hartree-Fock calculation increases with N^5, where N is the system size (the number of basis functions).[3] The largest computational overhead is related to the calculation of the Fock

[3]There are other drawbacks inherent to Hartree-Fock calculations, such as the poor description of single-particle states and the complete absence of electron correlations [112].

matrix, the many-body Hamiltonian of a system of N identical particles [106]. On the one hand the use of Slater- or Gaussian-type orbitals reduces this computational overhead since many of the single and two-body integrals may be performed analytically. On the other hand, the number of Gaussian functions necessary for a good description of each orbital is relatively large.

An extension to the Hartree-Fock method is an approach known as Configuration Interaction [114], where an appropriate linear combination of Slater determinants is used, including a number of orbitals describing excited states. However, wavefunction-based methods such as these are prohibitively expensive except for relatively small systems. In large scale atomic calculations where one deals with hundreds or perhaps thousands of atoms, and where translational symmetry may be broken, a new approach is required; a formulation of quantum mechanics that significantly reduces the number of variables, but still enables us to calculate electronic properties with high degrees of accuracy.

2.2 Density Functional Theory

One possible way of tackling the many-body problem in terms of one particle wave functions is offered by Density Functional Theory (DFT) [112, 115]. In 1964, Hohenberg and Kohn [77] demonstrated a theorem in which the problem of finding the many-body wavefunction is reduced to that of calculating the equilibrium charge density $n(\vec{\mathbf{x}})$. The Hohenberg-Kohn theorem states that the ground-state energy E of an N-electron system is an unique functional of the charge density n,

$$E = E[n] = \hat{T}[n] + \hat{V}_{\text{ext}}[n] + \hat{V}_{Ne}[n] + \hat{V}_{ee}[n], \tag{2.13}$$

where we define the charge density n as

$$n^{\sigma_1}(\vec{\mathbf{r}}_1) = N_e \int |\Psi^e(\vec{\mathbf{x}}_1, \vec{\mathbf{x}}_2, \ldots, \vec{\mathbf{x}}_{N_e})|^2 \, d\sigma_2 d\sigma_3 \ldots d\sigma_{N_e} d\vec{\mathbf{r}}_2 d\vec{\mathbf{r}}_3 \ldots d\vec{\mathbf{r}}_{N_e}, \tag{2.14}$$

$$n(\vec{\mathbf{r}}) = \int n^{\sigma}(\vec{\mathbf{r}}) \, d\sigma = n^{\uparrow}(\vec{\mathbf{r}}) + n^{\downarrow}(\vec{\mathbf{r}}) \tag{2.15}$$

provided

$$\langle \Psi^e \mid \Psi^e \rangle = 1 \tag{2.16}$$

and

$$\int n^{\sigma}(\vec{\mathbf{r}}) \, d\sigma d\vec{\mathbf{r}} = N_e. \tag{2.17}$$

Moreover, the ground state density minimises such a functional.

The four terms on the right hand-side of equation (2.13) make up for the kinetic energy $\hat{T}$, the external applied electric field $\hat{V}_{\text{ext}}$ as well as the electron-nucleus and electron-electron interaction ($\hat{V}_{eN}$ and $\hat{V}_{ee}$ respectively).

Once the ground state charge density has been determined all ground-state quantities describing the system, such as the many-particle wavefunction are also univocally determined.

It is interesting to note that DFT is a completely novel formulation of quantum mechanics. Previously one would consider either the Hamiltonian or the Lagrangian formulations. In the former case, the wavefunction is the quantity sought. This could be obtained by either solving the wave equation (Schrödinger's formalism) or by diagonalising a Hamiltonian and solving the eigenvalue problem (Heisenberg). In the later case, the Lagrangian formulation, one seeks to minimise the action in order to find the propagation of a particular state. Both formulations have been shown by Feynman to be equivalent [116].

For time-independent problems[4] DFT provides yet another approach where the main quantity we are interested in is the classical electron charge density. In this case the number of parameters involved is reduced to three (the value of the charge density in real-space) whereas in the two cases discussed above one needs to deal with the coordinates of each particle.

Hence, if the density functional is known we will be able to solve the variational problem for the electron density and obtain all the ground-state properties of our system. Unfortunately, the exact functional is not known and the Hohenberg-Kohn theorem alone does not provide a procedure on how to find the ground state charge density. Therefore one must rely on approximations.

In 1965, Kohn and Sham [78] assumed that the problem of finding the ground state charge density can be mapped onto that of solving a set of single particle Schrödinger-like equations:

$$\left[-\frac{\hbar^2}{2m}\nabla^2 + V_{\text{eff}}\left(\vec{\mathbf{x}}\right)\right]\psi_i\left(\vec{\mathbf{x}}\right) = \epsilon_i\psi_i\left(\vec{\mathbf{x}}\right). \tag{2.18}$$

The set of eigen-states $\{\psi_i\}$ which are solutions to the above eigenvalue problem are known as Kohn-Sham states. The effective potential V_{eff} corresponds to the effective single particle potential seen by an electron due to its interaction with the

[4] An analogous version to the Hohenberg-Kohn theorem was developed to include time-dependent potentials. This is known as the Runge-Gross theorem [117]. This way one can calculate optical excitations in atoms and molecules in the adiabatic limit [118].

other $N-1$ Kohn-Sham states.[5] This potential is defined as

$$V_{\text{eff}}\left(\vec{\mathbf{x}}\right) = V\left(\vec{\mathbf{x}}\right) + V_H\left(\vec{\mathbf{x}}\right) + V_{XC}\left(\vec{\mathbf{x}}\right). \tag{2.19}$$

The first term in equation (2.19) is the external potential and includes the potential originating from the nuclei as well as an external applied electric field if present. The term V_H corresponds to the classical Coulomb potential (Hartree potential) for an electron density $n\left(\vec{\mathbf{r}}\right)$. This term is obtained by solving the Poisson equation for the scalar potential

$$-\nabla^2 V_H\left(\vec{\mathbf{r}}\right) = n\left(\vec{\mathbf{r}}\right). \tag{2.20}$$

Finally,

$$V_{XC}\left(\vec{\mathbf{x}}\right) = \frac{\delta E_{\text{XC}}}{\delta n} \tag{2.21}$$

is the exchange-correlation potential defined as the functional derivative of the exchange-correlation energy, E_{XC} with respect to the electron density. This last term contains all the remaining contributions to the potential that we do not know exactly. Finally, the total energy of the system is given by the sum over all the occupied states of the Kohn-Sham (KS) single particle energies ϵ_i up to the total number of electrons N_e,

$$E_{\text{Tot}} = \sum_{i}^{N_e} \epsilon_i. \tag{2.22}$$

Consequently we define the Fermi energy for this system as the highest occupied Kohn-Sham eigenvalue, ϵ_{N_e}. Furthermore one can generalise equation (2.22) to include temperature

$$E_{\text{Tot}} = \sum_{i} f\left(\epsilon_i - E_{\text{F}}\right)\epsilon_i \tag{2.23}$$

with the Fermi distribution f defined in (1.17).

The Kohn-Sham eigenfunctions $\{\psi_i\left(\vec{\mathbf{x}}\right)\}$ can be used to calculate n,

$$n\left(\vec{\mathbf{r}}\right) = \sum_{i}^{occupied} \left|\psi_i\left(\vec{\mathbf{r}}\right)\right|^2 = \sum_{i} \left|\psi_i\left(\vec{\mathbf{r}}\right)\right|^2 f_i, \tag{2.24}$$

where f_i is the occupation number ($0 \leq f_i \leq 1$) and provided that

$$\langle \psi_i \,|\, \psi_i \rangle = 1. \tag{2.25}$$

The solutions of the Kohn-Sham equations in principle give the ground state properties of the system. However, the term described in equation (2.21) is not know

[5] In practice, "standard" DFT methods also include spurious interactions of the electron with its own charge density. This effect is know as the self-interaction (SI) and can be important for strongly-correlated systems [86].

exactly and some kind of approximation is needed. The two types of approximations which are generally used are the local density approximation[6][7] (LDA) [78, 121] and the generalised gradient approximation (GGA) [122, 123, 124]. In the first case, one considers E_{XC} to be that of a uniform electron gas of the partial density $n(\vec{\mathbf{r}})$. Within this approximation, the exchange and correlation energy is given by

$$E_{XC}^{LSDA} = \int d^3r \;\; n(\vec{\mathbf{r}})\, e_{xc}\left(n^{\uparrow}, n^{\downarrow}\right), \tag{2.26}$$

where e_{xc} is the exchange-correlation energy density (energy per unit volume) for a uniform electron gas [125, 126]. In equation (2.26) we take the more general spin polarised case by introducing different charge populations for spin *up* ($\uparrow$) and spin *down* ($\downarrow$) whereby the total charge density is defined as the sum of the two (Eq. (2.15)).

The second case is an extension of the former and introduces terms depending on the gradient of the charge density. One of the forms used for V_{XC} in GGA is the Perdew-Burke-Ernzerhof (PBE) form [124]

$$E_{XC}^{GGA} = \int d^3r \mathcal{F}\left(n^{\uparrow}, n^{\downarrow}, \nabla n^{\uparrow}, \nabla n^{\downarrow}\right) \tag{2.27}$$

Note that both LDA and GGA are local approximations while the exact exchange-correlation potential may be non-local.

These choices of V_{XC} have been widely used in a variety of problems ranging from semi-conductors to metals, from solids to molecules. Today, density functional theory is widely employed in the description of bulk materials and molecules in physics, chemistry, biology and even geology. These approximations usually yield reasonably good bond lengths. In particular, GGA is widely used in chemistry to calculate bond lengths in organic molecules and reaction paths with great success [127, 128].

While in the chemical sciences GGA consistently gives more accurate results the same is not true in physics and materials science. In some cases, albeit being a cruder approximation, LDA results compare better to experiments (usually in the case of simple metals where the density is uniform).

Finally, we end this section with a few notes on the Kohn-Sham orbitals, the eigenstates $\psi_i(\mathrm{r})$ of equation (2.18). Strictly speaking, these orbitals are not single-particle states. Therefore they can not be interpreted as molecular orbitals of our

[6]Local spin density approximation (LSDA) in the case of spin polarised systems.

[7]Recently the issue of uniqueness of the spin-polarised LDA (LSDA) potentials has come into question, although the uniqueness is recovered in the case of non-collinear spins. It is not the aim of this work to discuss these issues here. The reader should refer to [119, 120] and references therein.

many-body problem. Moreover, DFT, as mentioned earlier, is a ground state theory. Despite these claims, the calculation of band structures, both conduction and valence, and molecular energy levels using DFT-based Hamiltonians is widespread in the scientific community and in many cases, it yields accurate results. Therefore, one must always be aware of such limitations when dealing with DFT calculations.

To a large extent the electronic transport properties of nanoscopic systems is determined by three factors: the band structure of the electrodes, the position of the energy levels of the scattering region and the level alignment between the two. Therefore, we can, for practical purposes associate the accuracy of a transport calculation using DFT Hamiltonians to the accuracy of band structure calculations and/or molecular energy levels.

2.2.1 Limitations of LDA and GGA

Despite the success of density functional theory and the reasonably accurate descriptions obtained using LDA and GGA there are a number of problems for which these approximations fail. In some cases the discrepancies between experimentally obtained properties and DFT calculations are so large that they hinder even a qualitative analysis of the results. One of the most notorious cases is that of the transition metal oxides. Take for example the case of bulk nickel oxide (NiO). LDA calculations yield a metallic ground state whereas experiments show that it is an anti-ferromagnetic Mott insulator [129]. Figure (2.1) shows the real magnetic configuration of NiO in the rock-salt structure. In the ground state AF2 magnetic phase atoms align ferromagnetically within [111] planes and antiferromagnetically between the planes.

In both LDA and GGA, the exchange-correlation potential is a local functional of the charge density. Furthermore, they are accurate when the charge density is a smoothly varying function. Hence, for systems where strong correlation effects are important, *i. e.*, where the charge density changes sharply, these approximations most likely fail.

Anisimov *et al.* [130, 131] proposed a correction, based on the Hubbard model. The general idea is to correct for localisation effects by replacing the LDA XC energy with the Hubbard-U energy (a function of the Coulomb repulsion parameter U and the exchange parameter J) that depends on the orbital occupations. The authors postulated the correction which needs to be added to the total LDA energy

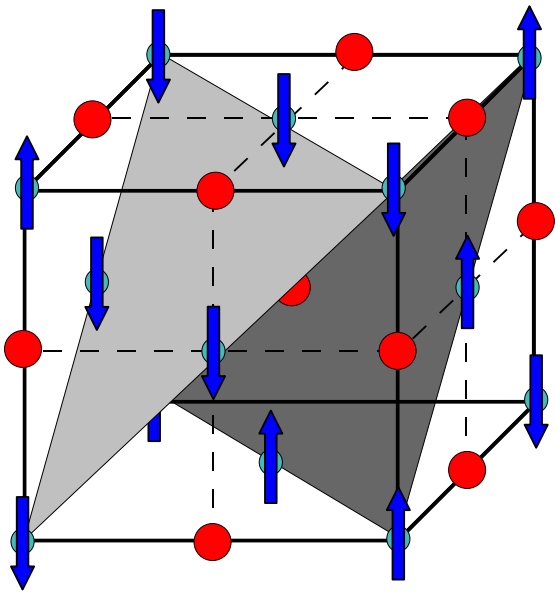

Figure 2.1: Schematic representation of rock-salt NiO in the AF2 anti-ferromagnetic configuration. The oxygen atoms are represented as red spheres and the Ni atoms as blue arrows pointing in the direction of the local magnetisation. The Ni atoms are ferromagnetically aligned within the [111] planes of the structure whereas the coupling between planes is anti-ferromagnetic.

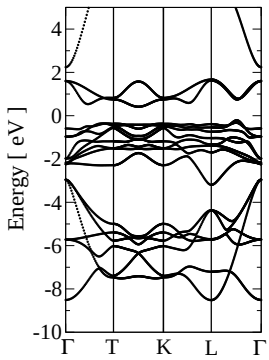

Figure 2.2: Band structure of bulk NiO using density functional theory in the local spin density approximation in the AF2 magnetic configuration. Majority and minority spin bands are identical.

$$\Delta E = \frac{1}{2}\sum_{m,m',\sigma} U n_{m\sigma} n_{m'-\sigma} + \frac{1}{2}\sum_{m,m',\sigma} (U-J)\, n_{m\sigma} n_{m'\sigma} - U\left[N^{\uparrow}\left(N^{\uparrow}-1\right)/2 + N^{\downarrow}\left(N^{\downarrow}-1\right)/2 + N^{\uparrow}N^{\downarrow}\right] + J\left[N^{\uparrow}\left(N^{\uparrow}-1\right)/2 + N^{\downarrow}\left(N^{\downarrow}-1\right)/2\right], \quad (2.28)$$

where $N^{\uparrow}$ ($N^{\downarrow}$) is the total number of spin-up (spin-down) electrons and $n_{m\sigma}$ is

the self-consistent occupation for each state with spin σ ($\sigma =\uparrow, \downarrow$) and m quantum number (for d shells $m = \{-2, 2\}$). In the same way, the correction to the LDA potential is of the form

$$\Delta V_m\sigma = U \sum_{m'} \left(n_{m'-\sigma} - n^0_{-\sigma}\right) + (U - J) \sum_{(m\neq m')} \left(n_{m'\sigma} - n^0_{\sigma}\right) + (U - J) \left(\frac{1}{2} - n^0_{\sigma}\right) \tag{2.29}$$

for each spin σ and quantum number m. Here $n^0\sigma$ is the average orbital occupations of the correlated shell

$$n^0_\sigma = \frac{1}{2l+1} N^\sigma, \tag{2.30}$$

and l is the orbital quantum number [132].

In principle, the correction can be applied to all the orbitals (in that case U and J would be matrices), but it is common to correct only the more localised orbitals such as the d and f shells. As Anisimov *et al.* note, U does not correspond exactly to the atomic Hubbard U term [133], because it also should include screening effects in the solid.

This method is usually referred to as the LDA+U method and depends on two parameters U and J which are usually fitted, *i. e.*, they are inputs to any calculation. Hence, one could claim that computations using a LDA+U functional are no longer fully *ab initio*. However, a physically appropriate choice of parameters leads to a good description of the electronic properties of strongly correlated materials such as the transition metal oxides.

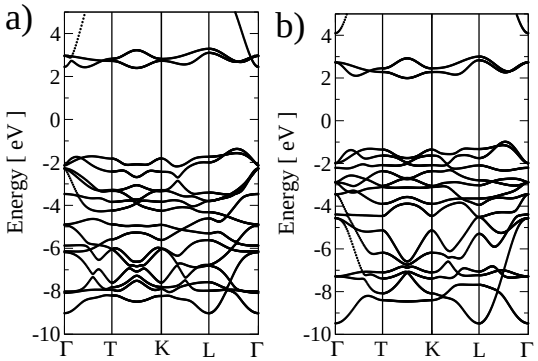

Figure 2.3: Band structure of bulk NiO using LSDA in the AF2 configuration using a) LDA+U and b) ASIC. In the antiferromagnetic case majority and minority band structures are identical.

An *ab initio* method for correcting the localised states comes in the form of self-interaction correction [125]. The effective potential (Hartree and exchange-correlation potentials) of equation (2.18) in both LDA and GGA include an integral

over the charge density. Therefore the effective potential seen by an electron includes the contributions of all the other electrons, but it also includes interactions with itself (the self-interaction). Perdew and Zunger [125] proposed a scheme for removing the contribution coming from the electron's SI by using the Kohn-Sham orbitals. This approach works well for molecules, however, in the limit of infinite systems, such as solids, such correction should go to zero (the self-interaction of a Bloch state vanishes for $N \to \infty$).[8]

A novel approach was proposed by Filippetti and Spaldin [134] where the correction is introduced as atomic corrections instead, an approximation that reduces the computational overhead and in the case of solids gives quantitatively satisfactory results [86]. Hereafter we shall refer to this approach as Atomic-SIC (ASIC). In both the cases of the Perdew-Zunger method as well as ASIC, there are no phenomenological parameters and it is a fully first-principles approach.

In figure (2.3) we show the results for the LDA+U ($U = 8$ eV and $J = 1$ eV) and ASIC methods. We can clearly see that in both cases the gap opens with respect to the LDA gap in the anti-ferromagnetic case (approximately 4 eV), and gets closer to experimental observations.

There are also functionals, where part (B3LYP) or all (EXX) of the exchange term from the Hartree-Fock method replaces the LDA term (keeping the correlation term intact). For a review see [113] and references therein.

2.2.2 The calculation of the Kohn-Sham states

So far we have not discussed the method for calculating the Kohn-Sham states ψ_i. One possible approach is to directly solve the Schrödinger-like Kohn-Sham wave equation (2.18) using a real-space approach [118, 135], *i. e.*, writing the wavefunction and Hamiltonian over some numerical grid.

Another possibility is to write the Kohn-Sham orbitals over a given basis set. Using a linear combination of basis functions the problem reduces to that of finding the expansion coefficients that minimise equation (2.18). One possible choice of basis set is a combination of plane waves [136]

$$\psi_i(\vec{\mathbf{r}}) = \sum_{\mathbf{k}} A_i^{(\mathbf{k})} e^{\mathbf{k}\cdot\vec{\mathbf{r}}}.^{9} \tag{2.31}$$

[8] In practice, for solids, the Perdew-Zunger approach over-corrects band gaps and other electronic properties of the system.

[9] The reader should be aware that the $\mathbf{k}$ vectors presented in equation (2.31) are not the momentum quantum numbers arising from Bloch's theorem for translationally invariant systems.

where usually one sums over as many **k** vectors as one deems necessary to appropriately describe ψ_i. Plane-waves might seem a natural since it is equivalent to a complex Fourier expansion of the real-space wavefunction. Due to this property the problem can be treated in reciprocal space using many of the properties of Fourier transforms [137]. In addition, the availability of the fast Fourier transform algorithm [101] makes calculations rather efficient in practice. Moreover, there is only one parameter controlling the quality of the basis set namely the maximum number of **k** vectors used. This obviously depends on the specific calculation and varies according to the system under study. The larger the number of vectors the more accurate the calculation, but also the more memory and numerically intensive it is.

A drawback of using plane-waves is its requirement of a large number of basis functions in order to describe localised states. Moreover, plane-wave codes describe the vacuum (a region where there is no charge density) on the same footing as the molecule. Hence, calculations of large scale molecular systems is hindered in plane-wave numerical implementations of DFT.

A possible way around this problem is that of using a localised basis. These can be Gaussian- or Slater-type orbitals or they can be made to resemble even more an atomic character. The KS orbitals are expanded as

$$\psi_i(\vec{\mathbf{r}}) = \sum_l c_l^i \phi_l(\vec{\mathbf{r}}) \tag{2.32}$$

where $\{\phi_l(\mathbf{r})\}$ is a set of functions with an atomic character. For example, for a H_2 molecule we would choose our basis functions as the solutions of the isolated atom centred on both hydrogens.

There are a number of advantages in using a localised basis set. One of these is that the range of interaction is finite, consequently Hamiltonian matrix elements go to zero for orbitals that are far apart. Therefore the Hamiltonian and overlap matrix, $S_{ij} = \langle \phi_i | \phi_j \rangle$ become relatively sparse saving memory and computer time.

Another important point will be discussed in section (2.4). The Hamiltonian and Overlap matrices in a localised basis representation are in a tight-binding-like form, very much the form needed by the NEGF formalism presented in chapter 1.

This choice of basis set is exactly the one made in SIESTA (Spanish Initiative for Electronic Structure Calculations with Thousands of Atoms) [40, 138], our DFT program of choice for electronic structure calculations.

2.3 The SIESTA code

There are a number of robust packages already available for doing DFT calculations. It is not the scope of this project to produce a new package for DFT, but possibly to introduce changes to an existing one in order to allow us to perform non-equilibrium transport calculations. The SIESTA code [40] appears as a reasonable choice because it is based on a localised basis set and it is readily available. It is important to note, however, that the NEGF framework (and in particular our implementation of it) is more general, *i. e.*, it does not depend on the choice of DFT package. In fact, the Hamiltonian used need not be the one originating from DFT, it could for example be a tight-binding Hamiltonian [70] or even a many-body one [139, 140]. On the other hand, the Kohn-Sham Hamiltonian seems like a natural choice because the total energy and the Hamiltonian are written in terms of the charge density and consequently the density matrix, a quantity that is readily available in the NEGF formalism (equation (1.43)). Furthermore, a DFT implementation based on an LCAO basis set is consistent with the derivation of NEGF described in chapter 1.

The basis set in SIESTA is a numerical basis obtained by solving the Schrödinger equation of the isolated atom immersed in a hard-wall potential. It reads

$$\phi_{n,l,m}(r,\theta,\varphi) = R_{n,l}(r)\, Y_{l,m}(\theta,\varphi) \tag{2.33}$$

where $R_{n,l}$ is the radial function for orbital n and $Y_{l,m}$ is the real spherical harmonic for the orbital angular momentum l and magnetic quantum number m.[10] The radial part of the wave function satisfies the normalisation relation

$$\int |R_{n,l}(r)|^2 r^2 dr = 1. \tag{2.34}$$

Most of the time, we are interested in the properties stemming only from the outermost electrons in the atom.[11] One possible approximation is to separate the core electrons (the electrons closest to the nucleus) from the valence electrons. In that case, the potential as seen from the valence electrons is that of the nucleus screened by the core electrons. The so called pseudopotential [141] is not only much smoother than the all-electron potential (it does go as $1/r$ for $r \to 0$), but it also enables us to focus on a reduced number of particles for our problem. Hence, the

[10] Both the radial and angular parts of the wavefunctions are real, hence so is the basis function ϕ.

[11] One can consider that the bonding, electronic and transport properties of materials are mostly influenced by valence electrons.

basis set $\{\phi_i\}$ where $i = \{n, l, m\}$, characterises only a subset of electrons in a given atom, for example $3d$ and $4s$ in Nickel. The remaining electrons are accounted for in the pseudopotential [141].

The pseudopontetial is initially written in semi-local form (a different radial potential for each angular momentum) and then it is transformed to its full non-local form as proposed by Kleinman and Bylander [142].

In order to achieve the necessary variational freedom, one can also include empty orbitals (say $4p$ in Ni). Moreover SIESTA also includes the possibility of using a multiple-ζ basis set. Each ζ orbital retains the same spherical harmonics as the original atomic orbital, but the radial form is given by a new function constructed with the split-valence method [143]. Using this method, the radial part of our second-ζ retains the tail of the first-ζ outside a split-radius r_l^s and has a polynomial form inside:

$$R_{n,l}^{2\zeta} = \begin{cases} r^l \left(a_l - b_l r^2\right) & \text{if } r < r_l^s \\ R_{n,l}^{1\zeta}(r) & \text{if } r \geq r_l^s \end{cases} . \tag{2.35}$$

The constants a_l and b_l are determined by matching the wavefunction and its first derivative.

The opposite is also possible. The radial function $R(r)_{n,l}$ remains unchanged while one takes the spherical harmonics with higher orbital angular momentum. These are known as polarised orbitals.[12]

$$\phi_{n,l',m} = R_{n,l} Y_{l+1,m}, \tag{2.36}$$

with $-(l+1) < m < l+1$. These extra basis functions enlarge the variational freedom in the minimisation procedure and allow one to construct basis functions with an angular momentum larger than the largest allowed by the pseudopotential. Usually, the dimension of the basis set is larger than the total number of electrons (in the case the number of basis functions equals that of valence electrons we talk about the "minimal" basis function).

Figure (2.4) shows the radial part of different basis functions for a Ni atom. We can clearly see that the wavefunctions go to zero for $r > r_c$, the cutoff *radius*.[13] This property ensures the sparsity of the Hamiltonian.

The overlap matrix is defined as

$$S_{ij} = \int d\vec{\mathbf{r}}\ \phi_{i'}\left(\vec{\mathbf{r}} - \vec{\mathbf{R}}_I\right) \phi_{j'}\left(\vec{\mathbf{r}} - \vec{\mathbf{R}}_J\right) \tag{2.37}$$

[12]The corrections to the basis function due to a constant electric field in first order perturbation theory will only have angular momentum components $l' = l \pm 1$. These polarised orbitals help to account for changes in the orbitals due to bond formation.

[13]The cutoff radius r_c can be different for each orbital.

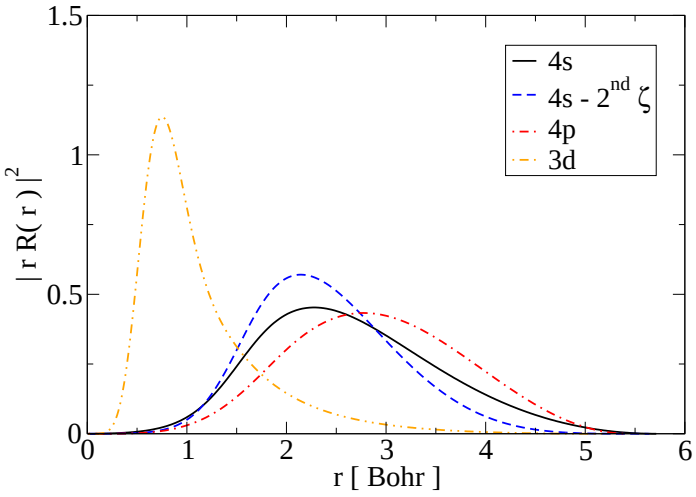

Figure 2.4: Numerical localised atomic orbital basis set for Ni generated by SIESTA. For $r > r_c$ the cutoff radiae, the basis functions go to zero.

with $i = \{i', I\}$, $j = \{j', J\}$ and $\vec{\mathbf{R}}_I$ is the position of the $I - th$ atom.

Using an initial charge density n_0 (usually the charge density of the isolated atoms comprising the system), the potential is calculated in real space. The Hartree potential is calculated by solving the Poisson equation (2.20) in reciprocal space using a Fast Fourier Transform (FFT) algorithm. It requires the potential to be periodic, but it can make use of very efficient optimised FFT methods. The exchange and correlation potential can be calculated using either (2.26) or (2.27), and (2.21).

Once the potential has been obtained, the Kohn-Sham Hamiltonian matrix is computed by evaluating integrals of the form

$$\begin{aligned} H_{ij} &= -\frac{\hbar}{2m}\int d\vec{\mathbf{r}}\ \phi_i\left(\vec{\mathbf{r}}-\vec{\mathbf{R}}_I\right)\nabla^2\phi_j\left(\vec{\mathbf{r}}-\vec{\mathbf{R}}_J\right)+ \\ &+ \int d\mathbf{r}\ \phi_i\left(\vec{\mathbf{r}}-\vec{\mathbf{R}}_I\right)V_{\text{eff}}\left(\vec{\mathbf{r}}\right)\phi_j\left(\vec{\mathbf{r}}-\vec{\mathbf{R}}_J\right). \end{aligned} \tag{2.38}$$

For periodic systems, one must also include the coupling to the periodic mirrors of the unit cell

$$H_{ij}\left(\vec{\mathbf{k}}\right) = \sum_l H_{ij}^l e^{i\vec{\mathbf{k}}\cdot\vec{\mathbf{r}}_l}, \tag{2.39}$$

where $\vec{\mathbf{r}}_l$ is the position vector between the 0-th and the l-th unit cells. An analogous equation can be written for the total overlap matrix S.

The Hamiltonian is then diagonalised to obtain the coefficients c_l^i for the $i - th$ eigenvector ψ_i as defined in equation (2.32).

Once the Kohn-Sham eigenvectors

$$\psi_i(\vec{\mathbf{r}}) = \sum_l c_l^i \phi_l(\vec{\mathbf{r}}) \tag{2.40}$$

have been calculated, the density matrix can be obtained

$$D = \sum_l^{N_{E_F}} |\psi_l\rangle\langle\psi_l| = \sum_l^{N_{E_F}} \sum_i \sum_j c_l^i c_l^{j*} |\phi_i\rangle\langle\phi_j| \,, \tag{2.41}$$

where N_{E_F} is the number of occupied states up to the Fermi level.

Therefore the matrix elements of the density matrix expressed over the localised basis set are equal to

$$D_{ij} = \sum_l c_l^i c_l^{j*} f(\epsilon_l - E_F) \,. \tag{2.42}$$

The electron charge density is just the diagonal elements of the density matrix in the real-space representation

$$\langle\vec{\mathbf{r}}|D|\vec{\mathbf{r}}\rangle = n(\vec{\mathbf{r}}) = \sum_{i,j} \phi_i(\vec{\mathbf{r}}) D_{ij} \phi_j(\vec{\mathbf{r}}) \,. \tag{2.43}$$

The steps presented above are iterated until a self-consistent solution for the charge density is obtained. In other words, we start with a initial charge density n_0 which is used to calculate the effective potential $V_{\text{eff}}(\vec{\mathbf{r}})$. We then calculate the Hamiltonian elements H_{ij}. By diagonalising this Hamiltonian we find the KS eigenstates $|\psi_l\rangle$ which provide a new density matrix calculated using equation (2.41). This density matrix is subsequently projected onto the basis set to calculate a new electron charge density n_1. This procedure is repeated until the convergence criteria is satisfied

$$||n^j - n^{j+1}|| < \delta, \tag{2.44}$$

where δ is a tolerance parameter.

Recently there have been a number of extensions to SIESTA such as the inclusion of different approximations for the exchange-correlation potential (LDA+U [132] and SIC [86]) and Spin-Orbit interaction [109].

Although SIESTA is a state of the art DFT package, it cannot treat open systems, *i. e.*, it can only treat finite or periodic Hamiltonians. If one wishes to calculate the transport properties of devices using density functional theory, a novel approach must be taken to evaluate the electronic structure of an infinite non-periodic system. Most importantly, one must avoid the problem of diagonalising the Kohn-Sham Hamiltonian, which in the case of an open system is infinite.

2.4 *Smeagol*: electronic transport at the atomic and molecular scale

So far we have presented two seemingly dissimilar theoretical frameworks. On the one hand the method presented in chapter (1) deals with the electronic transport problem for an open system. The method itself is very general and up to this point no assumption was made about the character of the single-particle Hamiltonian $\mathcal{H}$ appearing in equation (1.1) except that it is a function of the charge density.

On the other hand, we have just presented the DFT formalism where the electronic structure of extended periodic systems and finite molecules can be calculated. The limitations of present implementations include their inability of treating systems with no translational invariance and the effects of an external electric field; and consequently it is impossible to calculate the electronic transport properties of devices.

Therefore it is natural to interface the two formalisms into a single tool. In other words, use density functional theory to calculate a single-particle tight-binding-like Hamiltonian and then use the NEGF formalism for obtaining the associated non-equilibrium density matrix which includes the effects of the semi-infinite leads as well as the external bias.

As we discussed in section (2.3) SIESTA is readily available as a DFT tool, it produces a single-particle Kohn-Sham Hamiltonian in a localised basis representation and it is capable of treating large scale systems ($>$ 100 atoms). The same cannot be said about an implementation of NEGF; a numerical tool which is versatile and which can treat the transport properties of many classes of problems was not yet available.

Hence we set out to develop *Smeagol* [71, 72], a computer software which uses DFT-NEGF to accurately predict the electronic transport properties of molecular devices [87], heterostructures [144] and tunnelling junctions [145] to name but a few.

In many cases we are interested in the magnetotransport properties, therefore

one must also be able to treat spin-polarised systems satisfactorily. This is also one of the main goals of *Smeagol*. One of its features is the calculation of the surface Green function using a semi-analytic approach and the solution of the K_1 problem (section (1.6)).

While SIESTA provides the Kohn-Sham Hamiltonian, *Smeagol* has been made to interface with it and to calculate the non-equilibrium charge density of an open system via Green functions.

In order to interface SIESTA with our transport code we need to make three major changes. First, we must include in our calculations the fact that our system is connected to semi-infinite leads on either side instead of being periodic. This can be done by simply adding the self-energies described in equations (1.34) and (1.35) to the KS Hamiltonian. These self-energies are obtained by a separate calculation for an infinitely long system as sketched in figure (1.10) and described in subsection (1.6.1). The Hamiltonian and Overlap matrix elements for each PL and their respective coupling terms between each PL are saved and subsequently read - during the *Smeagol* calculation - to calculate the surface Green function and the self-energies for a given range of energies. These terms are stored either in memory or on disk for future use. This clearly assumes that the leads are not affected by changes of the electronic structure of the scattering region when bias is applied.

The second change has to do with the Hartree potential, the classical electrostatic part of the energy functional. We must introduce a linear external potential associated with the external bias. The solution of the Poisson equation (equation (2.20) is defined up to a linear term. This term is determined by the boundary conditions at the edges of the cell. In our case, we wish to set the potential on the left- and right-hand-side boundaries to match those of bulk (the electrodes) plus a shifted induced by the external potential.

$$V_H(\vec{\mathbf{x}}) = \begin{cases} \frac{V}{2} + \phi_{\text{bulk}}(0) & z = 0 \\ -\frac{V}{2} + \phi_{\text{bulk}}(0) & z = L \end{cases} \tag{2.45}$$

where L is the length of the cell and $\phi_{\text{bulk}}(0)$ is the Hartree potential of bulk at the edge of the PL. In this approximation the only effect of the external potential V on the leads is a global shift of the electronic structure.

Since total Hartree potential can be separated into a periodic part plus the desired slope a constant slope can be added separately. The periodic part ϕ_H can be solved using the same FFT method used by SIESTA while the slope is added afterwards

resulting in the total Hartree potential for a bias V

$$V_H(\mathbf{x}) = \phi_H(\mathbf{x}) + \frac{V}{L}(z-a) + b \tag{2.46}$$

where a corresponds to the centre of the cell and b sets the zero of $V_H(\mathbf{x})$.

Figure (2.5) shows a sketch of a general device described by *Smeagol*: the scattering region is enclosed by the dashed line. In practice, the ramp is included in the form of a saw-like potential. The inclusion of the self-energies accounts for the break in translational symmetry.

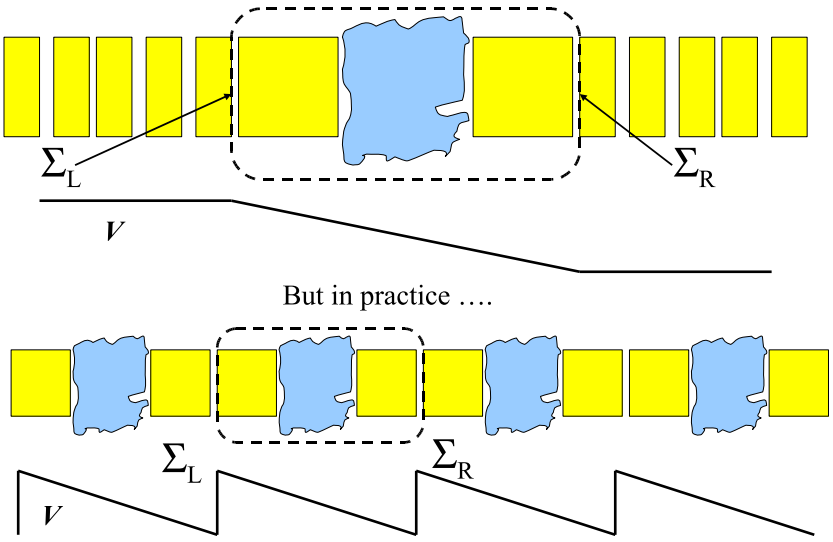

Figure 2.5: Real-space ramp added to the Hartree potential in SIESTA during the self-consistent cycle. a) The device described by *Smeagol*: one scattering region, two semi-infinite electrodes, and the bias across the extended molecule. Note that outside the interaction region the bias is constant. b) The way the electrostatic problem is solved in practice in SIESTA: a saw-like potential is added to V_H and the problem is solved using FFT's with periodic boundary conditions. Translational symmetry is broken by introducing the self-energies with the correct shift in the electronic structure.

Another change in the way the Hartree potential is handled is related to the constant b. The solution via FFT's discards the $\mathbf{k} = 0$ component of the Fourier transform which set the total charge in the cell. This means that in principle two different calculations might give different values for the constant b (V_H is obtained from the Poisson equation and can be rigidly shifted). This is not desirable because we need to match the potential at the edges of the cell to that of bulk. This issue is illustrated in figure (2.6) for a parallel plate gold capacitor compared to that of bulk gold. Here two infinite gold plates are set a distance of $\sim$ 12 Å apart. We

can see that moving away from the vacuum (central) region the system converges (the peak-to-peak oscillations remain constant) quite quickly. At the edges of the cell ($d = 0$ and 45 Å) the potential resembles that of bulk gold. However when we superimpose the two potential profiles we can clearly see a mismatch (indicated by the blue arrow in the graph). Because the total DFT potential is defined up to a constant we can, without loss of generality, impose a constant shift to the Hartree potential across the entire cell. This way, the potential at the edges of the cell match that of the bulk electrodes and we can introduce the self-energies from a separate calculation.

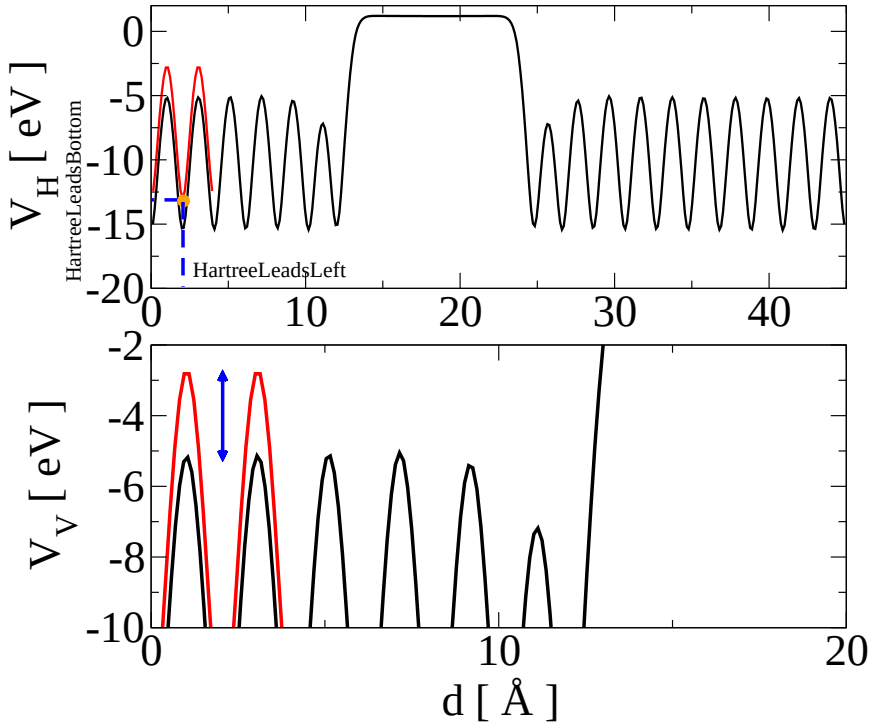

Figure 2.6: Hartree potential for a parallel plate capacitor (black line) and Hartree potential for one unit cell of bulk gold (red line). The blue arrow indicates the constant shift in the potential b which must be added to the calculation for the potential in electrodes and in the EM to match. Top and bottom panels represent the same figure with different scaling in the y axis.

In order to determine the constant b, a plane inside the scattering region is selected. The position of this plane along z is denoted *HartreeLeadsLeft* in figure (2.6) (a similar plane is selected for the right-hand-side denoted *HartreeLeasRight*). The potential for the electrodes is obtained from a separate calculation and the value of the potential is a parameter of the NEGF calculation. During the self-consistent

cycle the Hartree potential of the EM is calculated and the average value over the plane at HartreeLeadsLeft is compared to the one at an equivalent plane for the potential on the leads. The difference between these two values is deemed to be the value of b.

The third and final step consists in substituting the DFT procedure for calculating the density matrix with the NEGF technique. Once the Hamiltonians and overlap matrices are obtained, we can use our method to calculate the non-equilibrium density matrix using equation (1.43).

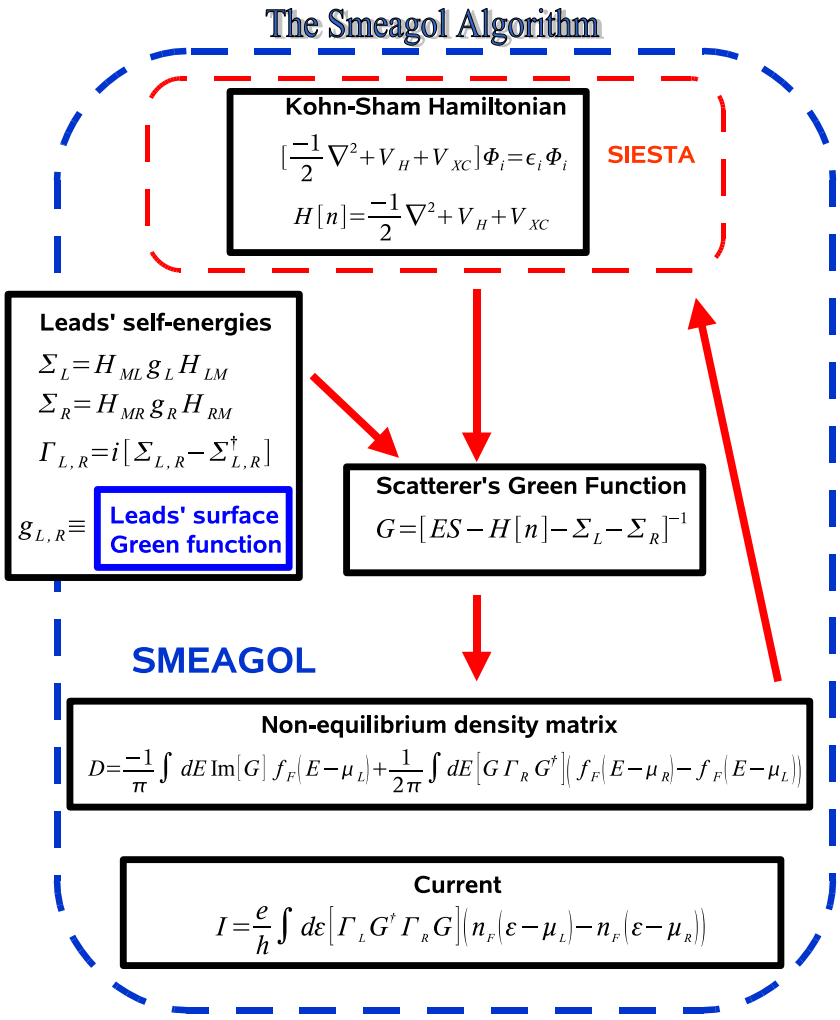

Figure 2.7: Flow-chart of the *Smeagol* program, highlighting the interconnection between *Smeagol* and SIESTA. It is clear that the code has been developed to interact with SIESTA in a modular fashion, making it portable to other *ab initio* computational tools.

In summary, we can calculate the density matrix for an open system within DFT and apply the method to a range of problems, for many different materials and geometries. Note that as far as the algorithm is constructed the specific form of the Hamiltonian is irrelevant, once it is written in a LCAO basis set and it is a functional of the charge density. *Smeagol*, in fact, is built in a modular fashion which gives us the option of using a different DFT software at the price of only minor changes. Hence interfacing *Smeagol* with other LCAO DFT codes or other Quantum Chemistry tools such as HF is relatively simple.

In figure (2.7) we show a general fluxogram of *Smeagol* and how it interfaces with SIESTA. We can clearly see that SIESTA provides the KS Hamiltonian and *Smeagol* introduces the self-energies turning the system from periodic to a central scattering region attached to semi-infinite electrodes. The codes exchange Hamiltonians and density matrices iteratively until self-consistency is achieved. Then *Smeagol* is used to calculate the transport properties such as the transmission coefficients and the $I-V$ characteristics.

2.4.1 Parallelising *Smeagol*

The systems we wish to deal with can be relatively large. Although SIESTA - and in general, other codes based on LCAOs - is generally less computationally intensive than plane wave codes, there are limits to the size of systems we can tackle on a simple workstation. These limitations can be either due to the memory needed or the time one is prepared to wait for a calculation to be performed.[14]

Either way, a parallel approach to SIESTA might solve the problem. SIESTA has been parallelised using the Message Passing Protocol (MPI) [146], so it can be used in most distributed memory clusters. The parallel version of SIESTA provides two types of parallelism: over k-points and over basis functions. In both cases the initial Hamiltonian in sparse form is distributed over all processors, improving memory usage.

For a periodic system we start by discretising the BZ into a set of k-points $\{k_i\}$. When the number of points is relatively large each processor solves the eigenvalue problem for equation

$$\left(\sum_{j=0}^{N} H_j e^{i\vec{\mathbf{k}}\cdot\vec{\mathbf{r}}_j} - E\sum_{j=0}^{N} S_j e^{i\vec{\mathbf{k}}\cdot\vec{\mathbf{r}}_j}\right) = 0 \tag{2.47}$$

[14] With present computational capabilities, one could treat a maximum of about 200 atoms on a single precessing unit.

in series using a different k-point. The resulting eigenvectors $|\psi_l^{k_i}\rangle$ and eigenvalues $\epsilon_l^{k_i}$ are then regrouped to perform the integral (sum) over k-points in equation the equation for the density matrix

$$D = \int_{\mathbf{k}} d\mathbf{k} \sum_i |\psi_i^{\mathbf{k}}\rangle\langle\psi_i^{\mathbf{k}}| \sim \frac{1}{V_{\mathrm{k}}} \sum_{\mathbf{k}}^{N_{\mathrm{k}}} \sum_i |\psi_i^{\mathbf{k}}\rangle\langle\psi_i^{\mathbf{k}}| \tag{2.48}$$

where N_{k} is the number of k-points used in discretising the reciprocal space (for solving the problem numerically) and V_{k} is the volume of the Brillouin zone (BZ). This method is known as parallel over k (POK). This form of parallelism is highly scalable; the number of point-to-point communications is relatively small and the total number of CPUs[15] can go up to a few hundred depending on the total number of k points. The main drawback of this method is that it requires the number of k-points to be bigger than the number of processors. For small systems, specially metals, the number of k-points can reach a few thousand, but for larger unit cells or molecules, where we have only one k-point, one must rely on a different kind of parallelism.

When the number of k points is smaller than the number of processors - for instance, a Γ point calculation - we perform the diagonalisation itself in parallel in what is known as the parallel over orbitals (POO) method. Unfortunately diagonalisation algorithms in parallel, in general, are not very efficient. The need for a large number of communication tags between CPUs leads to poor scalability specially in networks where the interconnects are slow, e.g. TPC/IP. At best, this type of parallelism, scales conveniently (around linear scaling) up to 6 CPUs for a TCP/IP network and 12-16 CPUs over Infiniband$^{\mathrm{TM}}$. Therefore, it is always preferable to use the POK whenever possible.

Diagrams of the two procedures are shown in figure (2.8). In the POK method the full Hamiltonian for each k-point is sent to a number of CPUs which is subsequently diagonalised and regrouped to calculate the density matrix. In the POO the Hamiltonian is diagonlised using a parallel algorithm (Scalapack [147]).

As mentioned in section (2.4), *Smeagol* bypasses the diagonalisation procedure by performing the integrals of equations (1.57) and (1.58). The main computational bottleneck in *Smeagol* is performing these integrals. This includes performing the matrix inversion in equation (1.33) for each energy. Numerically, an integral is nothing more than a sum. Therefore we can calculate each term of such sum independently in parallel and collect the results at the very end. This scheme is called parallel over energy (POE).

[15]The central processing unit (CPU) is commonly known as the processor.

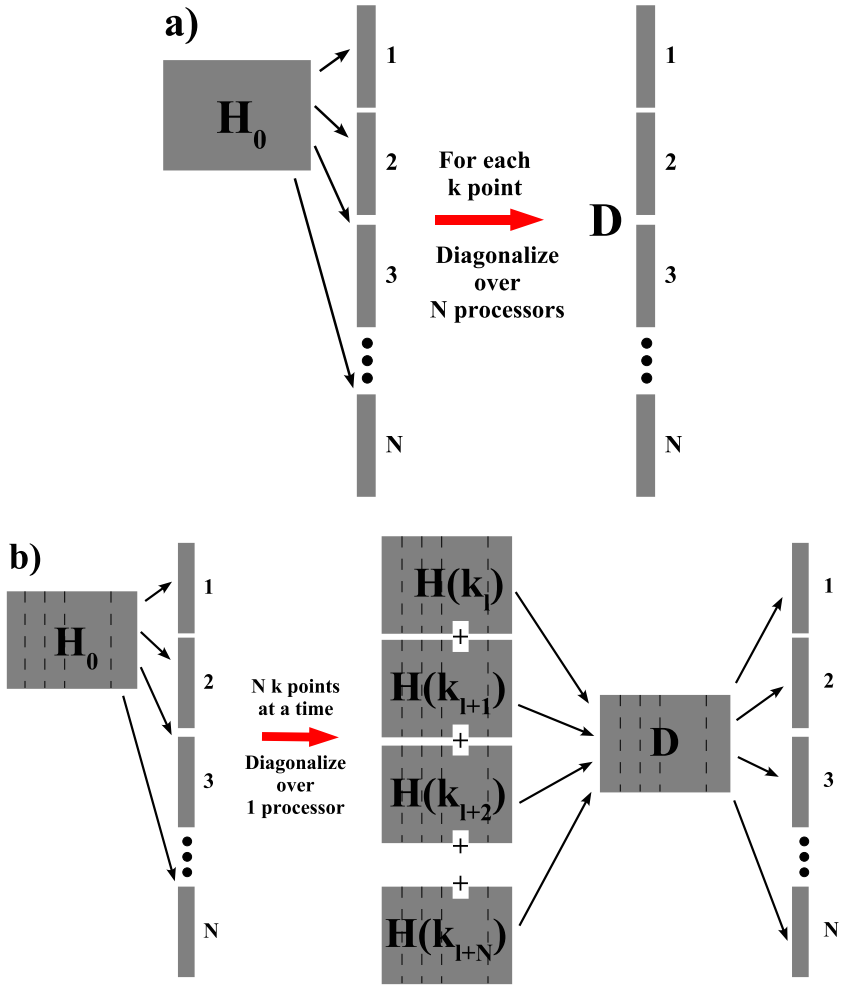

Figure 2.8: Two choices of parallelism in SIESTA. a) Parallel over orbitals (POO): the total Hamiltonian is diagonalised in parallel and the density matrix is calculate. b) Parallel over k-points (POK): the Hamiltonian for each k-point is diagonalised in series, each in a different CPU. The eigenvectors are regrouped to calculate the density matrix.

In many ways, this scheme is similar to the POK method whereby the inversion at each energy is calculated over a different processor and $D_{\mathrm{eq}}(E_i) + D_{\mathrm{V}}(E_i)$ is subsequently computed. Finally, once all the energy points have been calculated all the processors sum the results (with the appropriate weighting factors) to obtain the total density matrix.

In tables (2.1) and (2.2) we show how *Smeagol* scales as a function of the number of processors for two different types of interconnect.[16] We can clearly see how the to-

[16]The calculations were performed, in both cases, on AMD-64bit-Opteron clusters with 4 Gb

tal CPU time[17] remains relatively unchanged, an indication that the communication overhead is small. Consequently, as the number of processors increases the wall-time (the actual real time taken for the calculation) decreases almost as $1/N$. This is true for both types of interconnects (only slight differences are observed) which ensures good scalability (the slight increase in total wall-time is observed due to communication overheads). Most importantly there is no significant difference between different types of communication switches (in fact we observe better results using TCP/IP over Infiniband).

Although we observe a significant increase in the total CPU time ($\sim$ 26 %), the NEGF segment of the calculation only increases by approximately 10 %. This is mostly due to the calculation of the potential in real space. Firstly, with the increase in the number of processors the NEGF part of the calculation loses importance (from approximately 70 % to 50 % of the total time of the calculation). Secondly, the distribution of the grid over the processors can be controlled by the user. For consistency, the default values were set throughout, but the appropriate choice of parameters can lead to decreased communication between compute nodes and significant improvements in performance.

Number of CPUs / Time [s]	8	16	32	64
Total CPU Time	33951.188	26094.441	28490.203	33923.216
CPU Time NEGF subroutine	25771.792	21587.093	22871.922	25728.925
Total Wall-time	4243.898	1630.902	890.318	530.050
Wall-time NEGF subroutine	**3221.474**	**1349.193**	**714.747**	**402.01**

Table 2.1: Timing of *Smeagol* for k-point (4 k-points) calculation using 16, 32, 64 and 128 processors at 0 bias for a 85 atom unit cell ($N = 826$) over TCP/IP.

The *Smeagol* method can be easily parallelised up to 100 processors using the same scheme as in the parallel over k method. A description of a more scalable

of RAM per node (2 CPUs per node) and 2.3 GHz clock-speed. We used the Pathscale [148] compiler with the following compilation flags in both cases: *-m64 -mtune=opteron -mieee-fp -zerouv -OPT:Ofast -O2 -march=opteron -mcpu=opteron -ipa*.

[17]The CPU time corresponds to the sum over all processing units of the time taken for a set of operations

Number of CPUs / Time [s]	8	16	32	64
Total CPU Time [s]	29575.384	31497.067	36839.019	46331.667
CPU Time NEGF subroutine	21074.052	21876.695	23434.525	26718.410
Total Wall-time	3696.9	1968.6	1151.2	723.9
Wall-time NEGF subroutine	**2634.2**	**1367.2**	**732.3**	**417.4**

Table 2.2: Timing of *Smeagol* for k-point (4 k-points) calculation using 16, 32, 64 and 128 processors at 0 bias for a 85 atom unit cell ($N = 826$) over Inifiniband^{TM}.

method for parallelising *Smeagol* up to 4096 processors is presented in the appendix A.

2.4.2 An overview of *Smeagol* capabilities

As a tool for calculating accurate materials specific transport properties at the atomic scale, *Smeagol* has a number of features including but not limited to:

- The use of *ab initio* Hamiltonians expressed in a LCAO basis and the flexibility to use both DFT and HF methods.
- Full parallelisation in energy (POE) up to 128 processors (see appendix A for parallelisation up to 4096 processors - energy and orbital space).
- Fully spin polarised including non-collinear spins.
- Ability to calculate both molecules and surfaces: finite and periodic boundary conditions in the transverse direction (orthogonal to the transport).
- Ability to perform large scale calculations up to 100 atoms per processor.
- Inclusion of new exchange and correlation functionals such as LDA+U [85] and self-interaction corrected LDA [86].
- Ability to calculate currents and transmission coefficients with a high degree of accuracy (some results spam over fiver orders of magnitude; see chapter (4) for details).

2.5 Test Cases

This section is divided in five subsections, each one of them devised to show one of *Smeagol*'s capabilities. In the first subsection we deal with a parallel-plate capacitor with vacuum as a dielectric medium. This simulation clarifies how *Smeagol* deals with the Hartree potential. In subsection (2.5.3) we show calculations for magnetic materials (one of *Smeagol*'s main capabilities) and in particular we show how it is possible to address systems with non-collinear spins. In subsections (2.5.4) and (2.5.5) we turn to the more realistic problems of hydrogen-rich Platinum point contacts and organic molecules sandwiched by metallic electrodes. In both cases, there have been extensive experimental investigations and we show how *Smeagol* is capable of addressing some issues relating to these systems.

2.5.1 Au capacitor: Hartree potential and bias ramp

One important test for *Smeagol* is to check that the self-consistent Hartree potential is correctly obtained. For that purpose, we performed calculations for two semi-infinite gold surfaces separated by 12.27 Å, thus creating an ideal parallel plate capacitor.

The two gold surfaces are oriented along the (100) direction and the unit cell has only one atom in the cross section. The extended molecule comprises seven atomic planes in the direction of the transport, which is enough for achieving a good convergence of the Hartree potential (the Thomas-Fermi screening length in gold is $\sim$0.6 Å [149]). For the calculation we use 100 k-points in the full Brillouin zone in the transverse direction, a single zeta basis set for the s, p and d orbitals and standard local density approximation (LDA) of the exchange and correlation potential.

In figure (2.9) we present the planar average of the Hartree (electrostatic) potential V_{H}, the difference between the planar average of Hartree potential at finite bias and that at zero bias ΔV, and the difference $\Delta\rho$ between the planar average of the charge density along the direction of the transport for a given bias and that at zero bias. The quantities shown in the picture are those expected from the classical physics of a parallel plate capacitor. In the leads the electrostatic potential shows oscillations with a period corresponding to that of the separation between the gold planes, but with a constant average. In contrast in the vacuum region the potential is much higher, since there are no contributions from the nuclei, but it is uniform. If we eliminate the oscillations, by subtracting the zero bias potential from that obtained at finite bias (figure 2.9b), we obtain a constant potential profile in the leads and a linear drop in the vacuum region. Finally the macroscopic average of the charge

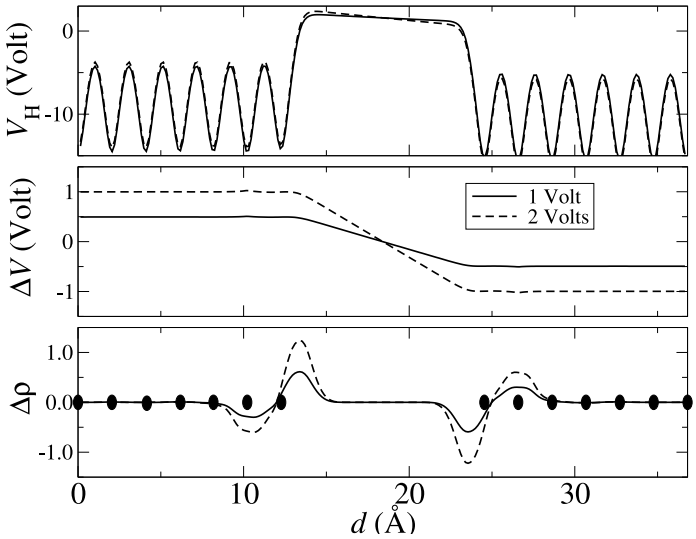

Figure 2.9: a) Planar average of the Hartree potential V_{H} for an infinite parallel-plate capacitor. b) Difference between the planar average of the Hartree potential at a given bias and that at zero bias ΔV. c) Difference $\Delta\rho$ between the planar average of the charge density along the direction of the transport for a given bias and that at zero bias. The dots indicates the position of gold planes.

density shows charge accumulation on the surfaces of the capacitor and local charge neutrality in the leads region as expected from a capacitor.

Similarly we can look at the equipotential surfaces in the vacuum region by plotting the iso-surfaces of constant potential along the central part of the capacitor. The result in shown in figure (2.10). We can clearly see that they represent planes parallel to the capacitor plates. Exactly as one would expect when the total electrostatic potential in the vacuum region is

$$V_H(\mathbf{r}) = V \cdot z \quad \forall x, y. \tag{2.49}$$

This result shows that the solution of the Hartree potential is consistent with the potential drop across a vacuum region of two infinite plates as described by classical electromagnetism [150]. Furthermore, we have shown that *Smeagol* can efficiently perform k-point calculations highlighting its potential for transport calculations through - magnetic or not - interfaces, a field of great interest [144, 145].

2.5.2 Au atomic chains

Metallic quantum point contacts (PC) present conductance quantisation behaviour even at room temperature [64, 151, 152, 153, 154]. While conductance quantisation

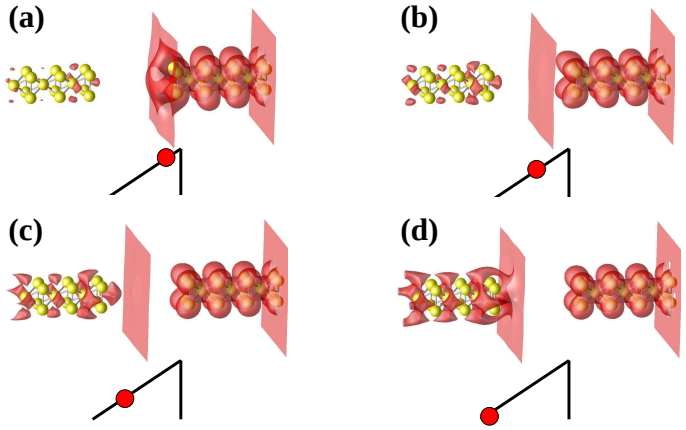

Figure 2.10: (a-d) Iso-surfaces of constant potential along the vacuum region of the capacitor for different positions perpendicular to the capacitor plates. For each panel we also present schematically the potential at which the iso-surface is calculated.

in semiconductor point contacts can be observed in constrictions a few hundred Angstroms wide [155, 156], the same effect can achieved in metallic systems only at the atomic scale. The quantisation of conductance arises in one-dimensional systems due to the cancellation of the Fermi velocity and the density of states in the expression for the conductance [84]. This depends only on the number of bands available in the constriction (up to the number of valence electrons). A system is said to be 1D when the width of the constricted region is comparable to the Fermi wavelength. In the case of semiconductors that would be 200 Å for GaAs and in the case of metals a few Angstroms ($\sim$ 5 Å for Gold). Hence, we can clearly see that observing such an effect in metallic systems entails measurements in atomically thin constrictions.

In break junction experiments [152], two metal surfaces are brought into contact and subsequently separated. During the elongation process and just before the junction rupture the conductance displays flat plateaus and abrupt jumps (step-like curves). The experiments are repeated a number of times and the results recorded. In order to show conductance quantisation in atomically thin PCs one uses histograms to obtain statistically representative data of transmission curves as a function of the elongation process [152]. These histograms are obtained by summing all the conductance curves recorded in the course of an experiment. The steps observed in conductance curves are displayed as peaks in the histogram. Proof that Au PCs present one quantum of conductance is given by a sharp peak at 1 $G_0 = 2e^2/h$.

Recently, Rodrigues *et al.* have shown that the crystallographic orientation of the tips plays an important role in the determination of the transport properties of

these PCs [154]. The authors used atomically resolved high resolution transmission electron microscopy (HRTEM) to image the elongation process of gold point contacts. It is clear from HRTEM images that the point contacts retain the crystallographic bulk structure (fcc in the case of gold).

Hence, the theoretical description of electronic transport in atomic chains must take into consideration atomistic aspects of the system: the correct arrangement of the atoms and an accurate description of the electronic properties. As an example we have performed calculations for a [100]-oriented gold quantum point contact (see inset of figure (2.11)). A single gold atom is trapped at its equilibrium position between two [100] fcc pyramids. This is the expected configuration for such a specific crystal orientation, and the configuration likely to form in breaking junction experiments [157] for small elongation of the junction. It has also been confirmed by atomic resolution TEM images [151, 154, 158]. In this case we have used LDA and a single zeta basis set for s, p and d orbitals. The unit cell of the extended molecule now contains 141 atoms (seven planes of the leads are included) and we consider periodic boundary conditions with 16 k-points in the 2-D Brillouin zone.

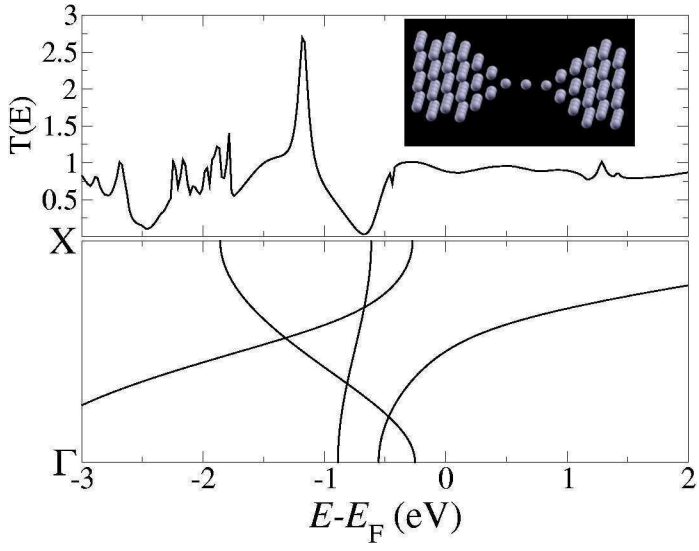

Figure 2.11: The transmission coefficient as a function of energy (upper panel) for a gold atomic point contact sandwiched between two gold tips oriented along the [100] direction. In the lower panel the band-structure for a monoatomic gold chain with lattice constant equal to the Au-Au separation in bulk gold. The inset shows a ball-and-stick representation of the atomic positions of the PC (the extended molecule).

In figure 2.11 we present the zero-bias transmission coefficient as a function of

energy. Recalling that the linear response conductance is simply $G = G_0 T(E_\mathrm{F})$ (in this case we have complete spin-degeneracy) our calculation shows one quantum conductance for this point contact. Interestingly the transmission coefficient is a rather smooth function $T \sim 1$ for a rather broad energy range around E_F. This means that the $G = 1G_0$ result is stable against the fluctuations of the position of the Fermi level, which may be encountered experimentally.

The large plateau at $T \sim 1$ (-0.5 eV $< E - E_F <$ 2 eV) indicates the presence of a single conductance channel for energies around and above E_F. This is expected from the band-structure of a straight monoatomic gold chain with lattice parameter equal to the Au-Au separation in bulk gold (see figure (2.11b)), which presents only one s band for such energy range. Therefore we conclude that the transport at the Fermi level is dominated by a single low-scattering s channel. Notably for energies 1 eV below E_F the transmission coefficient shows values exceeding one, which are due to contributions from d orbitals. In gold mono-atomic chains these are substantially closer to E_F than in bulk gold and participate to the transport. These results are in good agreement with previously reported calculations [92, 159] and experimental data [151, 152, 154]. Additional examples of *Smeagol*'s calculations for PCs carried out by the authors can be found in the next sections of this text and elsewhere in the literature [160, 161].

2.5.3 Nickel point contacts using non-collinear spins

The transport properties of magnetic transition metal point contacts have been the subject of several recent investigations [11, 162, 163, 164, 165, 166]. Technologically these systems are attractive since they can be used as building blocks for read heads in ultra-high density magnetic data storage devices. From a more fundamental point of view they offer the chance to investigate magnetotransport at the atomic level. Magnetic point contacts are effectively spin-valve-like devices, with the spacer now replaced by a narrow constriction where a sharp domain wall can nucleate [167].

A simple argument based on the assumption that all the valence electrons can be transmitted with $T \sim 1$ gives an upper bound for the GMR of the order of a few percent (250 % in the case of nickel). This however may be rather optimistic since one expects the d electrons to undergo quite severe back-scattering. Indeed small values of GMR for Ni point contacts have been measured [164]. Surprisingly at the same time other groups have measured huge GMR for the same system [11, 162, 168, 169]. Although mechanical effects can be behind these large values [165], the question on whether or not a large GMR of electronic origin can be found in magnetic point

contacts remains.

Therefore we investigate the zero bias conductance of a four atom long monoatomic Ni chain sandwiched between two Ni (001) surfaces (see figure (2.12)). This is an extreme situation rarely found in actual break junctions [170]. However an abrupt domain wall (one atomic spacing long) in a monoatomic chain is the smallest domain wall possible, and it is expected to show the larger GMR. For this reason our calculations represent an upper bound on the GMR obtainable in Ni only devices, and they also serve as a test of the *Smeagol* capability for dealing with non-collinear spins.

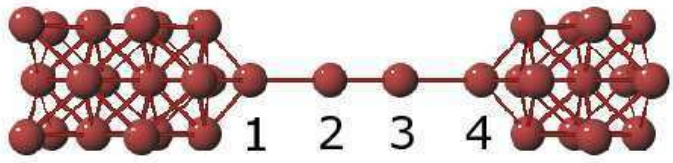

Figure 2.12: Schematic representation of the Ni point contact simulated. In the symmetric case the domain wall is located between the second and the third atom, while in the asymmetric it is placed between the third and the fourth. The direction of the current is from 1 to 4 for positive bias.

In this calculation we use a double zeta basis set for s, p and d orbitals and consider finite leads (no periodic boundary conditions are applied) with either four or five atoms in the cross section. We then investigate two possible situations. In the first one we place the domain wall symmetrically with respect to the leads, i.e. between the second and the third atom of the chain. In the second (asymmetric) the domain wall is positioned between the third and the fourth atom. Furthermore we perform spin-collinear and spin-non-collinear calculations for both cases. Interestingly all our non-collinear calculations always converge to a final collinear solution. This confirms expectations based on simple s-d model [171], suggesting that the strong exchange coupling between the conduction electrons and those responsible for the ferromagnetism, stabilise the collinear state if the magnetisation vectors of the leads are collinear.

In figure (2.13) we present the transmission coefficient as a function of the energy for both the symmetric and asymmetric case and the parallel state. For collinear calculations the contributions from majority and minority spins are plotted separately, while we have only one transmission coefficient in the non-collinear case. Clearly in

all the cases the non-collinear solution agrees closely with the collinear one, i.e.

$$T^{\uparrow}_{\text{collinear}} + T^{\downarrow}_{\text{collinear}} = T_{\text{non-collinear}}. \tag{2.50}$$

This is expected since the final magnetic arrangement of the non-collinear calculation is actually collinear, and it is a good test for our computational scheme.

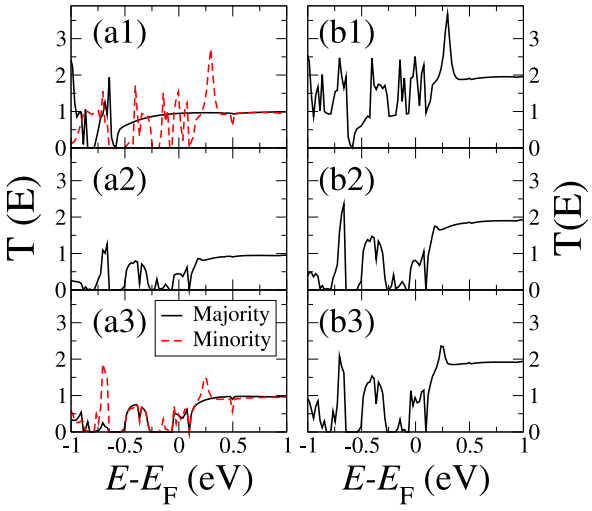

Figure 2.13: Transmission coefficient as a function of energy for the nickel quantum point contacts of figure 2.12. The right-hand side panels (a) are for collinear calculations and the left-hand-side (b) are for non-collinear; (1) parallel state, (2) antiparallel with symmetric domain wall, (3) antiparallel with asymmetric domain wall. Note that in the non-collinear case we do not distinguish between majority and minority spins. In panel (a2) majority and minority spins are degenerate.

Turning our attention to the features of the transmission coefficient it is evident that, at the Fermi level, T in the parallel state is larger than that in the antiparallel. This difference however is not large and the GMR ratio is about 60% with little difference between the symmetric and asymmetric domain wall. This is mainly due to the much higher transmission of the un-polarised s electrons compared with that of the d. Note that the conductance approaches $2e^2/h$ for energies approximately 0.5 eV above the Fermi level. For such energies in fact no d electrons contribute to the density of states of both the spin sub-bands, and only s electrons are left. These are then transmitted with $T \sim 1$ as in the case of Au chains investigated previously.

We will come back to the issue of large MR in magnetic point contacts in chapter 3 where we consider a number of magnetic configurations as well as impurities.

2.5.4 The importance of k-point sampling in Platinum single atom chains

The conductance of atomic metallic point contacts is an area of great interest. As we have discussed in the previous section, quantised conductance in metals was first observed in atomically thin gold nanowires. Since then a number of works have been performed over a number of different metals [172, 173].

Recently van Ruitenbeek *et al* [174] have performed experiments on Pt PCs in a hydrogen-rich environment. The authors observed a significant change in the transport behaviour when compared to *clean* conditions (cryogenic vacuum). For clean Pt point contacts a peak at 1.5 G_0 in the conductance histograms is predominant, but in a hydrogen-rich atmosphere a sharp peak at 1 G_0 appears instead. This is an indication that a H_2 molecule is bridging the gap between the two tips and it becomes the bottleneck that defines the transport properties of the whole system.

Despite indications that H_2 is bridging the point contact, it is impossible to experimentally probe the atomic arrangement of the molecules. Theoretical tools to model the molecule and calculate the transport properties come in hand for corroborating the assumption that the molecule actually lies between the two tips and for establishing the molecular orientation.

In order to address this issue we used *Smeagol* to perform calculations on Pt PCs. We used a double zeta basis set for both Pt and H. Our system consisted of two pyramidal tips connected by a hydrogen molecule. Initially we performed relaxations on the system by fixing the edges of the unit cell and allowing central region to relax. The total energy curve was calculated as a function of the unit cell size. We considered two configurations, namely the axis of the hydrogen molecule lying either along the axis of the tip - which we shall call bridge configuration (BC) - or perpendicular to it - called perpendicular configuration (PPC). Figure (2.14 shows the different atomic configurations in our calculations.

Figure (2.15) shows the total energy curve for different configurations of the hydrogen molecule on the tip as a function of distance between the two pyramids. We can see that, at small tip separations the hydrogen molecules remain dissociated in the pyramids instead of lying in between the two tips. That is clear from the lower energy for the CZ curve. As we simulate the pulling of the two tips - as we would expect in an STM or break junction experiment - a crossing point in which the BC becomes more energetically favourable can be seen. This trend seems to suggest that the Hydrogen molecule, as the tips are separated, tends move from the pyramids to the tips eventually lying along the axis of the point contact. This result, *i. e.* a

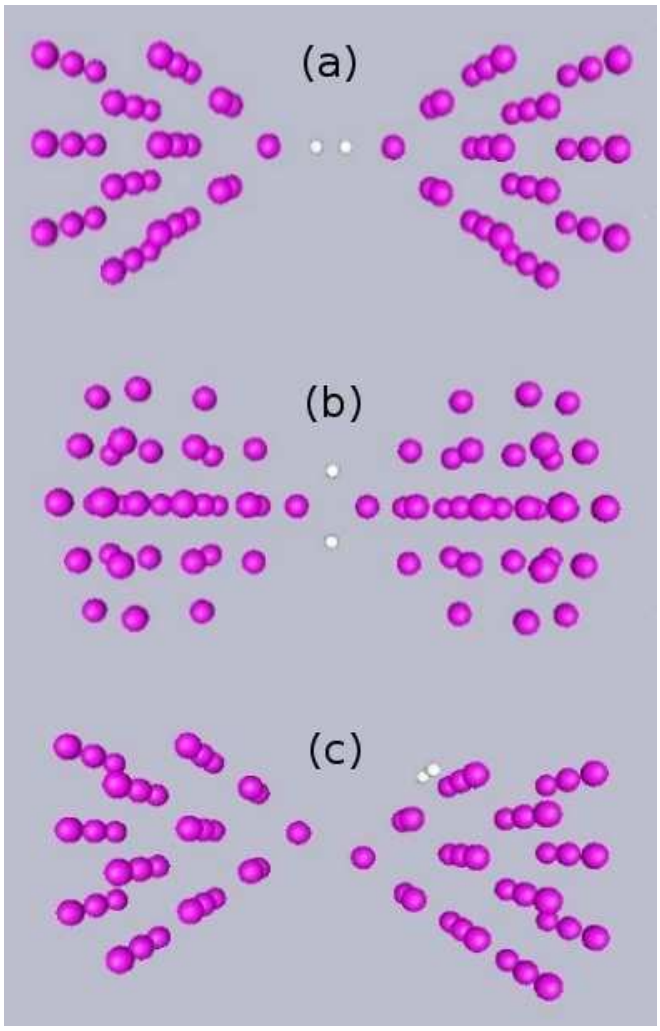

Figure 2.14: Sketch of a Platinum point contact with one hydrogen molecule in between the two tips. There are two possible configurations (a) bridge configuration (BC) and (b) perpendicular configuration (PC). c) We also consider the possibility that the H_2 molecule is adsorbed onto one of the tips (CZ).

configuration favouring the BC has also been obtained by other theoretical works [175, 176, 177].

In order to obtain the correct electronic structure of the electrodes, it is imperative to consider the boundary conditions along the transverse direction. Platinum, albeit non-magnetic, has d states which are close to the Fermi level. Therefore the band structure of bulk Pt has flat bands close to E_F. In order to ensure the correct description of these states we must use a reasonable k-point sampling in the transverse BZ. In figure (2.16) we show transmission curves for both the BC (fig.

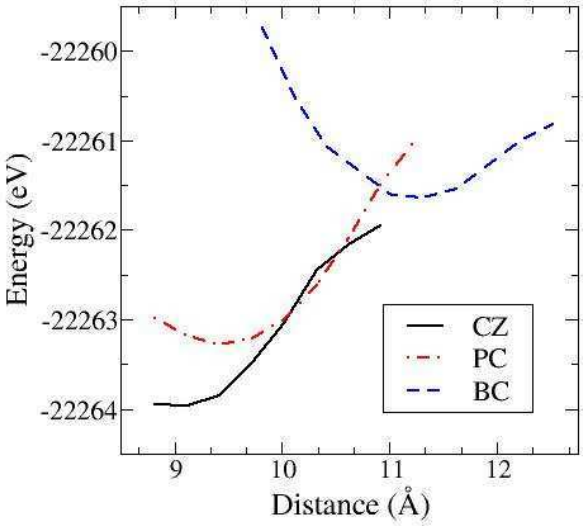

Figure 2.15: Total energy calculation for the relaxed system tip/H_2/tip. The solid (dashed) line represents the CZ (BC). The dotted-dashed line represents the PPC

(2.16a1-3)) and PPC (fig. (2.16b1-3)) using different sets of k-points. We can clearly see that as we introduce periodic boundary conditions and the number of k-points increases, the transmission curves become smoother. Finally, for 12 k-points the curves become sufficiently converged to the correct result.

For our calculations we use a double-ζ polarised basis set for platinum s, p and d orbital, a double zeta basis for the hydrogen s electrons and the LDA functional. As a first step we employ finite cross section leads along the transversal directions, composed of alternated planes containing 4 and 5 atoms each. The resulting transmission coefficients show many peaks and gaps throughout all the energy range and particularly sharp variations around the Fermi energy, as can be seen in figures 2.16 (a1) and (b1). When thicker slabs composed of alternating planes of 9 and 12 atoms are employed the results do not improve and the large oscillations still remain, as shown in figures 2.16 (a2) and (b2). It is apparent from these figures that while $T(E)$ shows a long plateau at positive energies, it presents strong oscillations at the Fermi energy and, therefore, it is uncertain to infer the conductance of the junction from $T(E_{\rm F})$.

This is in stark contrast with the case of gold, where the d-levels lie below $E_{\rm F}$, and $T(E)$ is smooth regardless of the size of the leads cross section. For platinum the presence of d-states at the Fermi energy opens mini-bands and mini-gaps, which translate into strong oscillations in $T(E \sim E_{\rm F})$. These mini-bands and mini-gaps

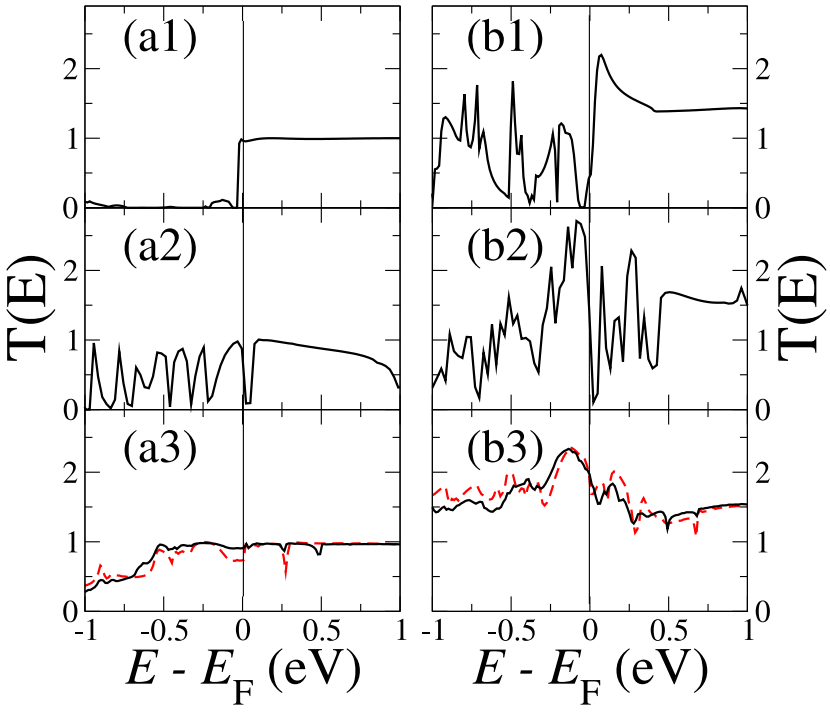

Figure 2.16: Transmission coefficients for an H_2 molecule sandwiched between fcc platinum leads near the equilibrium distances ($\sim$ 9.5 and 11 Å). The left hand side (a) corresponds to the configuration where the molecule lies parallel to the current flow and the right hand side (b) to the configuration where the molecule lies perpendicular. The leads are made of alternating slabs of 4-5 atoms (1) and 9-12 atoms (2) without periodic boundary conditions along the perpendicular directions (xy), and 9-9 atoms with periodic boundary conditions along xy (3). In the last case the dashed and continuous lines have been obtained with 4 and 12 k points, respectively.

arise from interference effects of the d-states along the transverse direction. Consequently, oscillations in $T(E)$ should disappear when bulk electrodes are used. Indeed, this is what we find when slabs made of 3×3 atomic planes and periodic boundary conditions are employed, as shown in figures 2.16 (a3) and (b3). We moreover show how $T(E)$ converges when the number of transverse k points is increased from 4 to 12. Although some small variations and peaks still remain when 4 k points are used, the transmission at the Fermi level is essentially converged. Note that the parallel case has $T \sim 1$ for a long range of energies around E_F, which remains essentially unperturbed for small variations of the coordinates or the distance between the electrodes. This explains the sharp peak observed in the experimental conductance histograms [174].

As we can see, in materials where d states play a role in the electronic proper-

ties, the correct calculation of the transmission coefficients involves using periodic boundary conditions. Moreover, we have shown that we can use *Smeagol* to solve experimental conundrums and provide useful insight into the world of metallic point contacts. Our point here was just to use an example of one possible *Smeagol* application. A more detailed description of this work can be found elsewhere [160, 161].

2.5.5 1,4-benzene-dithiolate on Au electrodes for molecular electronics applications.

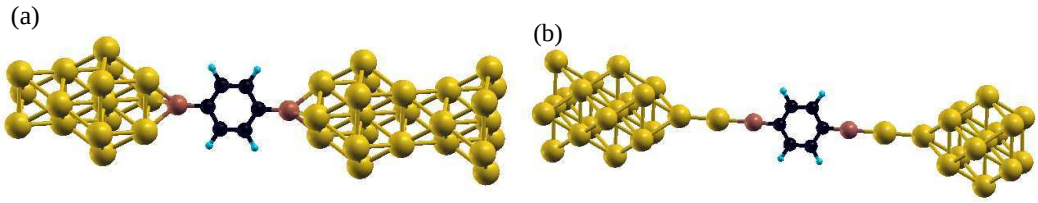

Figure 2.17: Ball-and-stick representation of a 1,4-benzene-dithiolate molecule attached to a a) [111] and b) [001] gold surface. Colour legend: C - black; H - light blue; S - red; Au - gold.

Recently there has been increasing interest in molecular electronics, *i. e.* in the ability to drive current through molecules and possibly their use as electronic devices. Integrating these devices could lead to applications ranging from sensors to new information data storage devices. The first experiments in molecular electronics were performed by Reed *et al.* [4]. The authors used a gold break junction setup to create a gap where a single 1,4-benzene-dithiol molecule (BDT) is trapped. A ball-and-stick model of the BDT molecule is shown in figure (2.17). The sulphur atoms (thiol groups) from both ends of the benzene ring bond strongly to the gold surface. The authors observed a strongly non-linear $I-V$ characteristics and a conductance gap of approximately 2 Volts.

After this seminal experiment many works in the field have followed, most of which use a similar set up with a choice of different organic molecules [27]. These experiments have shown interesting properties such as negative differential resistance [5], rectification [6] and transistor behaviour [7].

Partly due to the availability of experimental results, BDT attached to gold electrodes has become the benchmark for any transport calculation using *ab initio* methods [79, 99, 178]. All theoretical predictions give currents much higher (usually two orders of magnitude) than experimental observations. So far, no code has

been able to account for the differences in the conductance, but they all seem to give comparable results. This discrepancy has been so far attributed to our lack of knowledge about the atomic arrangement of the molecule and the tip. It has been argued that the position of the molecule on the gold surface has an effect on the transport properties.

We set out to perform our own calculations for benzene-dithiol using *Smeagol*. In particular, we wish to show how *Smeagol* can cope with the calculation of $I-V$ characteristics for different configurations of the electrodes. We have studied the effects of different surfaces, namely [111] and [001] on the $I-V$ characteristics of this molecule. In all cases we have modelled gold using a single-ζ s, p and d basis set whereas for both carbon and sulphur we used a double-ζ basis (s, p and d as well) with polarisation orbitals. Finally for hydrogen, a single-ζ polarised s wavefunction. In all cases finite boundary conditions were used.

The first situation considered was the case of a molecule attached to the hollow site in the [111] gold surface as our electrodes. Figure (2.17a) shows a ball-and-stick sketch of the system under consideration. The sulphur atom was positioned on the hollow site of the [111] surface of gold at distances according to values obtained in the literature for *ab initio* molecular dynamics calculations [179, 180].

As we apply a bias (see fig. (2.18)) we observe a small gap of about $0.5V$ before the onset of relatively high currents ($\sim 2\ \mu A$).

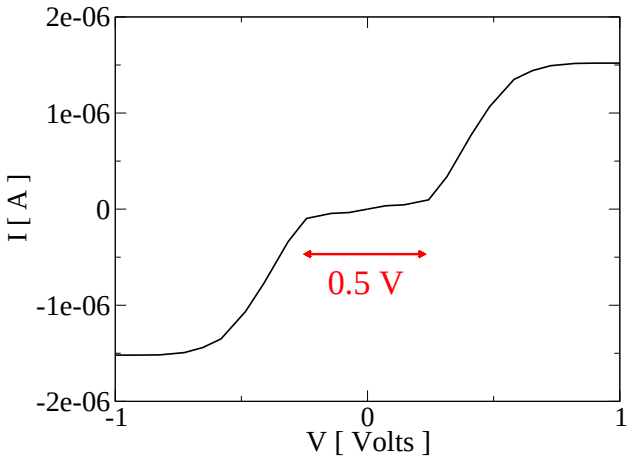

Figure 2.18: $I-V$ characteristics as a function of energy for different voltages for 1,4-benzene-dithiolate molecule attached to a [111] gold surface.

In figure (2.19) we present the transmission coefficients as a function of bias. We can clearly see that the transmission at zero bias (black curve) is quite small and there is a gap slightly bellow the Fermi level. Once we start to apply the bias the

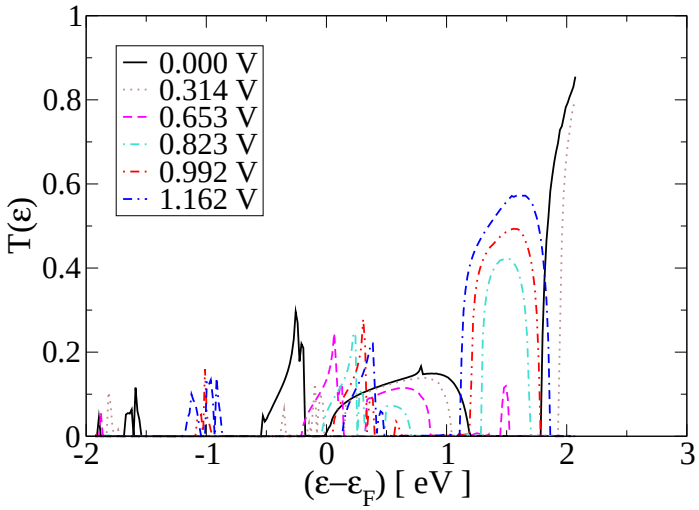

Figure 2.19: Transmission as a function of energy for different voltages for 1,4-benzene-dithiolate molecule attached to a [111] gold surface.

state positioned approximately -0.2 eV bellow the Fermi level starts to shift. Once the bias is sufficiently large ($\sim$ 250 meV) that state lies within the bias window and the system starts to conduct.

In the case of the [001] surface we place the sulphur atom on top of a single gold atom. This arrangement simulates a break junction experiment. While the two gold surfaces are being pulled apart gold atoms are removed from the surface forming a wire (the gold-gold bond is weaker than the gold-sulphur bond). Hence one expects the coupling to be quite different. In fact, the $I-V$ characteristics shown in figure (2.20) presents a different profile compared to the [111] case. From the onset of bias, the system is conducting, and there is no conductance gap around zero bias.

The reason for the discrepancy is clear if we look at the transmission coefficients for different bias presented in figure (2.21). At zero bias, the Fermi level is pinned to a resonance and, as one starts to apply bias, this state becomes immediately conducting. The transmission coefficient for such resonance is close to 1 G_0, the quantum of conductance, hence the currents for the [001] case are considerably larger than that in the previous case.

We can see that in both cases we have high conductance and in one particular case we see no gap at all. The explanation given earlier about the position of the atoms on the surface might seem likely at first, however, the experimental results seem quite robust. In particular, the typical gap observed in the experiments has also been measured in slightly different molecules [181]. One aspect not taken into account here

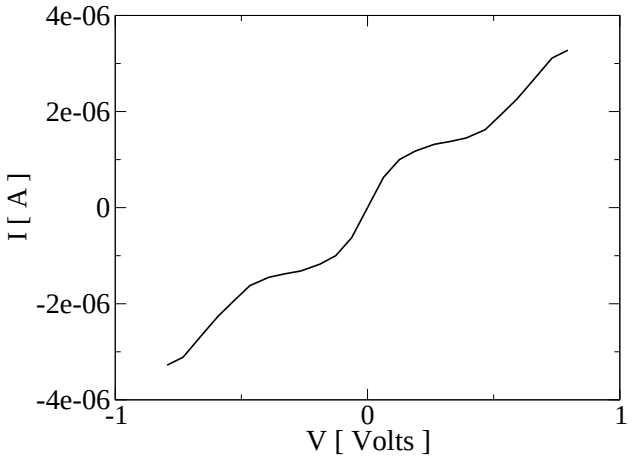

Figure 2.20: $I - V$ characteristics for 1,4-benzene-dithiolate molecule attached to a [001] gold surface.

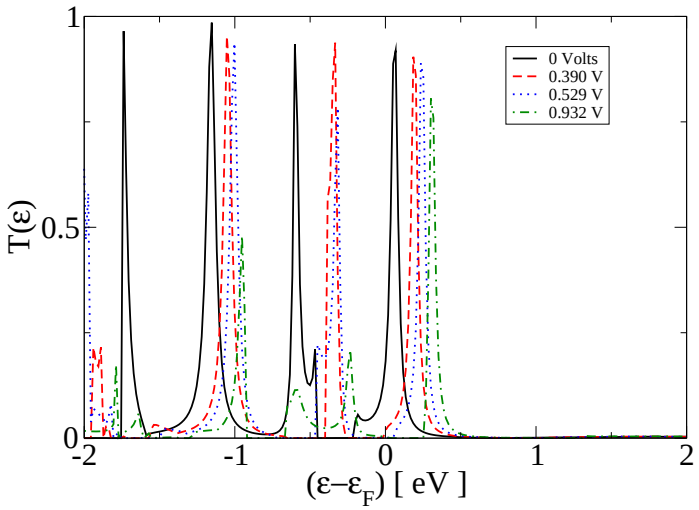

Figure 2.21: Transmission as a function of energy for different voltages for 1,4-benzene-dithiolate molecule attached to a [111] gold surface.

are the periodic boundary conditions, which might give rise to mini-gaps. However, other calculations including k-point sampling show similar behaviour [182].

A final comment on this issue is required. A possible explanation for the large disagreement between the experimental and theoretical results was given by Toher *et al.* [183]. The authors proposed that charging effects are not correctly taken into consideration by LDA and GGA because neither approximation possess the derivative discontinuity of the potential [182]. This mainly originates from the fact that LDA and GGA are not self-interaction free. This is of particular importance

in the case of weak coupling. In further work - using *Smeagol* - the authors showed that the energy levels of the self-interaction-corrected BDT molecule are driven down with respect to the Au Fermi energy. This in turn decreases the current.

More recent experimental data obtained in a more controlled set of experiments [27] seem to suggest that the conductance is higher than obtained by Reed and coworkers although still one order of magnitude smaller than theoretically predicted values. Results by Toher *et al.* are in reasonable agreement with this new set of results.

2.6 Conclusion

In this chapter we have presented the formalism for solving the ground state properties of a many-particle system using DFT. In particular, we have shown how DFT with an appropriate choice of exchange-correlation potential can give us an accurate description of the electronic structure of molecules and solids. Furthermore, we have shown how it is possible to take the Kohn-Sham Hamiltonian $H[n]$ - which is both a functional of the charge density and a single particle operator - and use it to calculate the non-equilibrium Green function and consequently the electronic transport properties of a nanoscopic system out of equilibrium (with an external bias applied).

The symbiotic relationship between DFT and NEGF has been realised within *Smeagol* our non-equilibrium electronic transport tool. We have highlighted *Smeagol*'s algorithm and main capabilities. We have presented how it interfaces with SIESTA, our choice of DFT code, and how it has been fully parallelised in order to cope with large scale computational problems in nanoscience.

As we have seen so far, *Smeagol* is a powerful tool. We can use it to perform calculations on a range of nanoscale systems. We have presented results on systems ranging from metallic point contacts to molecular electronic devices. In all cases we are able to obtain quantitative results that can be closely related to experimental observations and previous calculations.

In the next chapters we will use *Smeagol* to its full, exploring issues such as magnetic point contacts, molecular electronics using DNA and molecular spintronics, The latter is a field of particular interest to us because of our seminal work in the field [70, 88].